Journal of Materials Chemistry A

ROYAL SOCIETY OF CHEMISTRY

PAPER

View Article Online
View Journal

Cite this: DOI: 10.1039/d5ta03720d

Tailoring photocatalytic activity in porphyrin-MOFs: the role of amino-functionalized pillars in CO_2 adsorption and band structure modulation†

Xing-Zhe Guo,‡[a] Chi Cao,‡[b] Wei Liu,‡[a] Weiwei Xu,[a] Nan Ma,[a] Xiao-Xia Zhang,[c] Jinfa Chang [a] and Zihao Xing *[a]

The urgent need for sustainable carbon capture and conversion technologies has driven the development of advanced photocatalytic materials. Cobalt-porphyrin metal–organic frameworks (MOFs), engineered with tailored pore sizes, Lewis-basic functional groups, and optimized catalytic site densities, exhibit enhanced CO_2 adsorption capacity while facilitating efficient light harvesting and charge separation. Herein, we report two cobalt-based pillared-layer porphyrinic MOFs (TCPP-Pyz-Co and TCPP-NH_2Pyz-Co) designed for efficient CO_2 photoreduction. By incorporating amino-functionalized pillars, TCPP-NH_2Pyz-Co demonstrates a high CO_2 adsorption capacity of 82.8 $cm^3\ g^{-1}$ at 273 K. Furthermore, the introduced NH_2 groups narrow the bandgap and improve charge separation efficiency. As a result, TCPP-NH_2Pyz-Co achieves a remarkable CO production rate of 2221.4 $\mu mol\ g^{-1}\ h^{-1}$, surpassing that of TCPP-Pyz-Co (1807.6 $\mu mol\ g^{-1}\ h^{-1}$). Density functional theory (DFT) calculations reveal that the Co–Co paddlewheel nodes serve as the primary CO_2 adsorption sites, while the –COO group acts as an H_2O adsorption site. The amino functionality synergistically enhances CO_2 adsorption affinity due to the secondary sites in a position near to the primary CO_2 adsorption sites. This work underscores the pivotal role of Lewis-base functionalization in optimizing MOFs for dual CO_2 capture and conversion, providing a blueprint for next-generation photocatalysts.

Received 10th May 2025
Accepted 6th July 2025

DOI: 10.1039/d5ta03720d

rsc.li/materials-a

[a]Key Laboratory of Polyoxometalate and Reticular Material Chemistry of Ministry of Education, Faculty of Chemistry, Northeast Normal University, Changchun 130024, PR China. E-mail: xingzh612@nenu.edu.cn

[b]National Synchrotron Radiation Laboratory, University of Science and Technology of China, Hefei 230029, PR China

[c]School of Chemistry and Chemical Engineering, Fuyang Normal University, Fuyang 030008, PR China

† Electronic supplementary information (ESI) available. CCDC 2447987 and 2447985. For ESI and crystallographic data in CIF or other electronic format see DOI: https://doi.org/10.1039/d5ta03720d

‡ These authors contributed equally to this work.

Zihao Xing

Dr Zi-Hao Xing is an Associate Professor at Northeast Normal University. He was recognized as the Young Talent Lift Project in Jilin Province. Dr Xing graduated with a bachelor's degree in applied chemistry from Jilin University in 2013 and a PhD in Physical Chemistry in 2019. He conducted post-doctoral research at Shenzhen University from September 2019 to May 2022 and was a visiting scholar at Ilmenau University of Technology in Germany in 2020. His research focuses on the design and controlled synthesis of low-cost non-precious metal electrocatalysts for fuel cells; dynamic restructuring and catalytic mechanisms during electrocatalysis; and the photocatalytic performance of advanced materials such as MOFs and COFs. He has published over 30 papers in journals including J. Am. Chem. Soc., Angew. Chem. Int. Ed., Adv. Mater., Adv. Energy Mater.

Introduction

The increasing atmospheric concentration of carbon dioxide (CO_2), a major greenhouse gas, poses a severe threat to global climate stability, necessitating the urgent development of sustainable and efficient carbon capture and conversion technologies.[1–5] Among the various strategies under investigation, the photocatalytic CO_2 reduction reaction (CO_2RR), which utilizes solar energy to convert CO_2 into value-added fuels and chemicals, has emerged as a promising approach toward a circular carbon economy.[6–10]

The design of novel photocatalytic materials with enhanced performance and selectivity remains a crucial challenge.[11–13] Porphyrins, inspired by their central role in natural photosynthesis, exhibit strong visible-light absorption, long-lived excited states, and tunable redox potentials, making them ideal candidates for light-harvesting and catalytic applications.[14–18] Despite their potential, homogeneous porphyrin-based photocatalysts often suffer from aggregation, photobleaching, and difficulties in separation and recycling.[19–22] Porphyrin-MOFs, which integrate porphyrin units as organic linkers within a rigid framework, overcome these limitations by providing a stable and ordered environment that enhances light absorption, CO_2 diffusion, and catalytic efficiency.

In porphyrin-MOFs, the catalytic activity of cobalt centers can be finely tuned by the surrounding porphyrin ligands and the MOF architecture. The π-d orbital overlaps between porphyrin units and metal clusters facilitate electron transfer ability and suppress charge recombination, thereby improving CO_2RR activity.[23–25] To further enhance CO_2 conversion efficiency, it is essential to integrate Lewis-basic functional groups, which improve CO_2 adsorption with photocatalytic active sites during MOF construction.[26–30] Pillared-layer porphyrin-MOFs offer a versatile platform for such modifications, as their porosity and electronic band structure can be systematically tuned by incorporating Lewis-basic pillar ligands.[31–35] Thus, the rational design of cobalt-porphyrin MOFs with tailored pore environments, functional groups, and catalytic site densities is crucial for optimizing CO_2 adsorption, light harvesting, and charge separation, which are key factors in advancing heterogeneous CO_2 photocatalysts.

In this work, we synthesized two pillared-layer porphyrinic MOFs (TCPP-Pyz-Co and TCPP-NH_2Pyz-Co) by linking porphyrin carboxylic acid ligands with paddlewheel $Co_2(COO^-)_4$ clusters to form two-dimensional layers, bridged by pyrazine (Pyz) and aminopyrazine (NH_2Pyz) pillars. The introduction of Lewis-basic NH_2 groups modulates the pore environment and electronic band structure of the MOF. Compared to the non-functionalized analogue, TCPP-NH_2Pyz-Co exhibits a 20% increase in CO_2 uptake capacity. Moreover, the NH_2 groups optimize the local electron density and charge separation kinetics, significantly enhancing photocatalytic CO_2 reduction performance. Under visible-light irradiation, TCPP-NH_2Pyz-Co achieves a CO production rate of 2221.4 μmol g^{-1} h^{-1}, offering valuable insights for the design of high-performance photocatalysts.

Results and discussion

The cobalt-based pillared-layer porphyrinic MOF materials were self-assembled using *meso*-tetra(4-carboxyphenyl) porphine (H_4TCPP), $CoCl_2 \cdot 6H_2O$, and pyrazine (Pyz)/amino-pyrazine (NH_2Pyz) (Fig. S1†). As illustrated in Fig. 1a, the dinuclear Co(II) paddle-wheel nodes are linked by TCPP ligands to form two-dimensional (2D) square grids. These square grids are pillared by Pyz or NH_2Pyz ligands, which connect to the dinuclear Co(II) paddle-wheel nodes and the Co center of the porphyrin, forming a three-dimensional framework with a staggered arrangement as shown in Fig. 1b and c. Two cobalt-based pillared-layer single-crystal structures were confirmed by single crystal X-ray diffraction (SCXRD) (crystal data and structure refinement are provided in Table S1†) and optical micrographs (Fig. S2†). These MOFs were denoted as TCPP-Pyz-Co and TCPP-NH_2Pyz-Co. The simulated pore sizes of TCPP-Pyz-Co and TCPP-NH_2Pyz-Co, obtained using Mercury software, were 4.3 Å and 4.1 Å, respectively.

Powder X-ray diffraction (PXRD) and infrared (IR) spectroscopy (Fig. 1d, e and S3†) confirmed the successful synthesis of both MOFs. The experimental PXRD patterns matched the simulated results, indicating high phase purity. In TGA analysis (Fig. S4†), weight loss primarily occurs in three distinct stages: the first stage, observed below 300 °C, is attributed to the departure of residual solvent molecules from the framework material. The second stage occurring between 400 °C and 500 °C is the decomposition of the $Co_2(COO^-)_4$ clusters. Finally, the weight loss observed above 500 °C is ascribed to the collapse of the framework due to the degradation of the porphyrin ligands.[36]

The morphology and elemental distribution of TCPP-Pyz-Co and TCPP-NH_2Pyz-Co were characterized by scanning electron microscopy (SEM) (Fig. S5 and S6†). Both TCPP-Pyz-Co and TCPP-NH_2Pyz-Co exhibited block-like structures, with uniform distribution of C, N, O, and Co, as confirmed by energy-dispersive X-ray spectroscopy (EDS). X-ray photoelectron spectroscopy (XPS) further verified the presence of these elements, with peaks corresponding to Co 2p (781.8 eV), O 1s (531.8 eV), N 1s (399.8 eV), and C 1s (284.8 eV) (Fig. S7†). The Co 2p spectra of both TCPP-Pyz-Co and TCPP-NH_2Pyz-Co were deconvoluted into Co–O (797.0 eV for Co $2p_{1/2}$ and 781.3 eV for Co $2p_{3/2}$) and satellite peaks (802.3 eV and 785.1 eV). The O 1s spectra were resolved into Co–O (530.8 eV), C–O (531.7 eV) and C═O (530.1 eV). The N 1s spectra were divided into N–C (401.0 eV for TCPP-Pyz-Co and 400.5 eV for TCPP-NH_2Pyz-Co), pyrazine N (399.7 eV) and Co–N (398.8 eV), while the difference in binding energy of N–C is due to the introduced Lewis base –NH_2. Meanwhile, the C 1s spectra can be resolved into C═O (288.4 eV), C–O (286.5 eV), C–C (285.1 eV), C═C (284.5 eV) and C–N (284.0 eV). In addition, with the incorporation of amino functional groups, we further analyzed the N 1s spectra. The XPS peak area ratios for TCPP-Pyz-Co and TCPP-NH_2Pyz-Co are presented in Table S2.† A comprehensive analysis of the spectral areas reveals that upon introducing the NH_2 group, the content of C–N increased from 26.5% to 31.84%, whereas the contents of pyrazine-N and Co–N

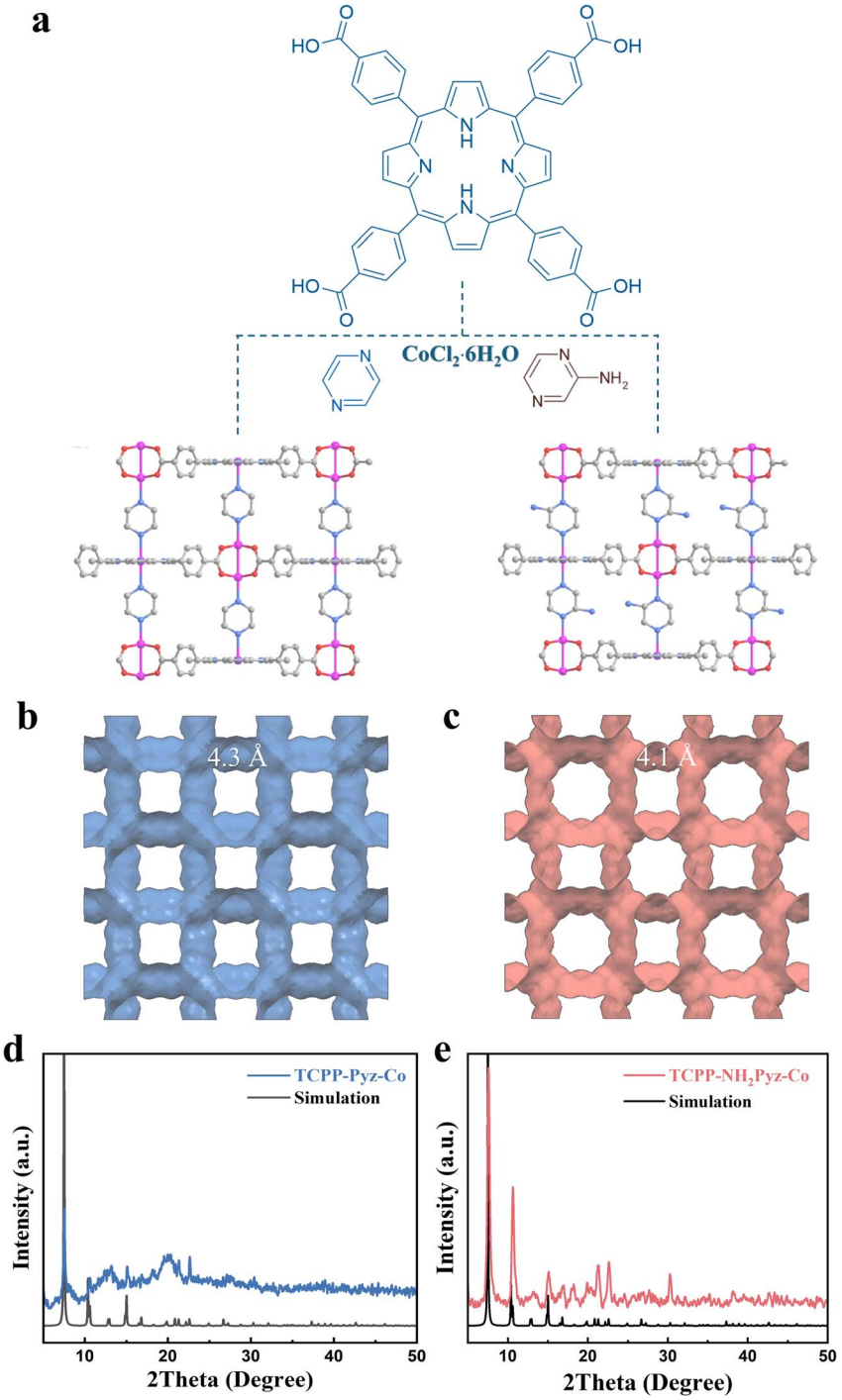

Fig. 1 Structures of pillared-layer (a) TCPP-Pyz-Co and TCPP-NH_2Pyz-Co. Pore structures of (b) TCPP-Pyz-Co and (c) TCPP-NH_2Pyz-Co. Powder X-ray diffraction patterns of (d) TCPP-Pyz-Co and (e) TCPP-NH_2Pyz-Co.

decreased slightly. These structural analyses confirmed the consistent framework integrity of both MOFs.

To investigate the influence of Pyz and NH_2Pyz ligands on the Co-porphyrinic MOFs, gas adsorption experiments were conducted (Fig. 2). N_2 adsorption isotherms at 77 K confirmed the permanent porosity of the samples (Fig. 2a). The pore sizes of TCPP-Pyz-Co and TCPP-NH_2Pyz-Co were approximately 3.7 Å and 3.9 Å, respectively, indicating their ultramicroporous nature (Fig. 2b). The measured pore sizes were slightly smaller than the theoretical values (Fig. 1b and c), likely due to residual non-activated solvents in the structure. The Brunauer–Emmett–Teller (BET) surface areas were 756 $m^2\ g^{-1}$ and 684 $m^2\ g^{-1}$ for TCPP-Pyz-Co and TCPP-NH_2Pyz-Co, respectively (Fig. 2c). The CO_2 adsorption studies revealed that the incorporation of Lewis-basic amino ($-NH_2$) functionalities significantly enhanced CO_2 uptake. At 273 K and 1 bar, TCPP-Pyz-Co and

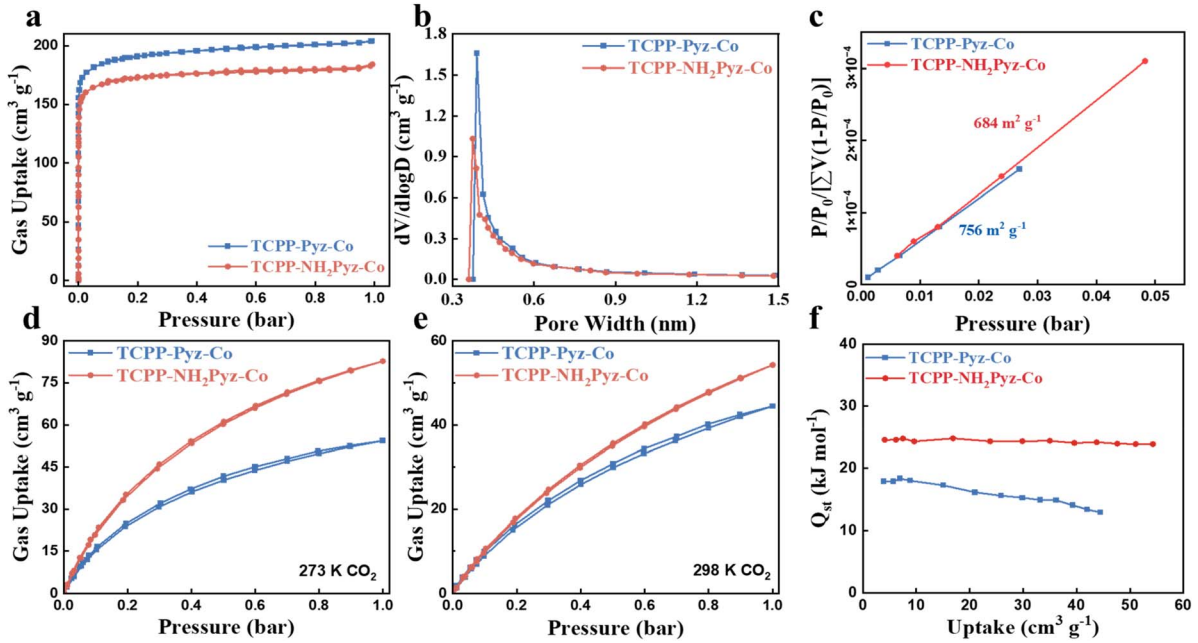

Fig. 2 (a) 77 K nitrogen adsorption isotherms of TCPP-Pyz-Co and TCPP-NH_2Pyz-Co. (b) Pore size distribution analysis of TCPP-Pyz-Co and TCPP-NH_2Pyz-Co. (c) BET specific surface area calculation of TCPP-Pyz-Co and TCPP-NH_2Pyz-Co. CO_2 adsorption isotherms of (d) TCPP-Pyz-Co and (e) TCPP-NH_2Pyz-Co at 273 K and 298 K. (f) Isosteric heat of adsorption on TCPP-Pyz-Co and TCPP-NH_2Pyz-Co.

TCPP-NH_2Pyz-Co exhibited a CO_2 adsorption capacity of 54.3 cm^3 g^{-1} and 82.8 cm^3 g^{-1}, respectively (Fig. 2d). Moreover, at 298 K and 1 bar, TCPP-NH_2Pyz-Co achieved a maximum CO_2 uptake of 54.3 cm^3 g^{-1}, compared to 44.5 cm^3 g^{-1} for TCPP-Pyz-Co (Fig. 2e). The isosteric adsorption enthalpy (Q_{st}) values were calculated to be 17.9 kJ mol^{-1} and 24.6 kJ mol^{-1} for TCPP-Pyz-Co and TCPP-NH_2Pyz-Co respectively, indicating strong CO_2 affinity for the –NH_2-functionalized framework (Fig. 2f). The

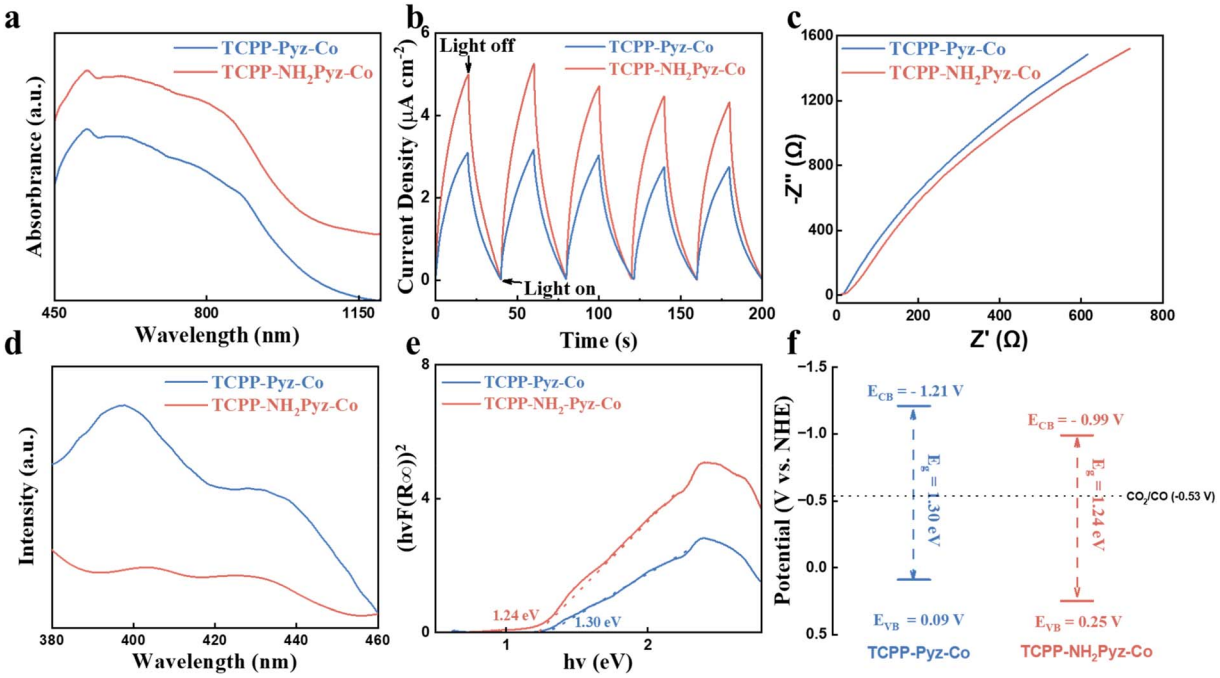

Fig. 3 (a) UV-vis diffuse reflectance spectra of TCPP-Pyz-Co and TCPP-NH_2Pyz-Co. (b) The photocurrent densities over TCPP-Pyz-Co and TCPP-NH_2Pyz-Co with the reaction time under chopped visible light illumination. (c) EIS analysis of TCPP-Pyz-Co and TCPP-NH_2Pyz-Co. (d) Photoluminescence spectroscopy spectra of TCPP-Pyz-Co and TCPP-NH_2Pyz-Co. (e) Tauc plots of TCPP-Pyz-Co and TCPP-NH_2Pyz-Co. (f) Schematics illustrating the energy band structures of TCPP-Pyz-Co and TCPP-NH_2Pyz-Co.

amino groups and organic linkers serve as high-affinity sites for CO_2 adsorption, with TCPP-NH_2Pyz-Co outperforming many recently reported MOFs (Table S3†).

The excellent CO_2 adsorption properties of these TCPP-Pyz-Co and TCPP-NH_2Pyz-Co make them promising candidates for light-driven CO_2 reduction. Photoelectrochemical characterization (Fig. 3) revealed strong light absorption in the range of 500 to 800 nm (Fig. 3a). TCPP-NH_2Pyz-Co exhibited a photocurrent response twice as strong as that of TCPP-Pyz-Co (Fig. 3b), suggesting enhanced carrier separation and transfer efficiency. Electrochemical impedance spectroscopy (EIS) Nyquist plots showed the smallest semicircle for TCPP-NH_2Pyz-Co (Fig. 3c), indicating faster charge transfer kinetics and charge separation. The strong charge separation capability of TCPP-NH_2Pyz-Co can also be validated through photoluminescence (PL) spectroscopy in which the PL intensity of TCPP-NH_2Pyz-Co was weaker than that of TCPP-Pyz-Co (Fig. 3d), further confirming improved separation of photogenerated electron–hole pairs in TCPP-NH_2Pyz-Co. The band structures of TCPP-Pyz-Co and TCPP-NH_2Pyz-Co were measured as shown in Fig. 3e and f. The band gaps for TCPP-Pyz-Co and TCPP-NH_2Pyz-Co were determined to be 1.30 eV and 1.24 eV (Fig. 3e), respectively, by Tauc plot analysis. The NH_2 groups narrowed the band gap of TCPP-NH_2Pyz-Co to broaden the light absorption. Meanwhile, Mott–Schottky plots were obtained to evaluate the semiconductor characteristics of the MOFs and their potential for photocatalytic CO_2 reduction at frequencies of 1500, 2000 and 2500 Hz, shown in Fig. S10.† The positive slopes observed in the plots confirm the n-type semiconducting behaviour of TCPP-Pyz-Co and TCPP-NH_2Pyz-Co. Herein, the flat band potentials (E_{fb}) (the flat-band potentials are typically equal to the conduction-band potentials in n-type semiconductors) for TCPP-Pyz-Co and TCPP-NH_2Pyz-Co were determined to be −1.21 V and −0.99 V *vs.* NHE respectively, which are more negative than the reduction potential of CO_2/CO (0.53 V *vs.* NHE). Meanwhile, the corresponding valence band maximum (VBM) values of TCPP-Pyz-Co and TCPP-NH_2Pyz-Co were calculated to be 0.09 V and 0.25 V *vs.* NHE (Fig. 3f). In light of these cumulative findings, we conclude that TCPP-Pyz-Co and TCPP-NH_2Pyz-Co function as promising photocatalysts in light-driven CO_2RR. The intrinsic structural design incorporating these ligands enables robust light absorption and efficient photon harvesting capabilities. Furthermore, the introduction of the Lewis base functionality in TCPP-NH_2Pyz-Co narrows the band gap to broaden the light absorption range to increase the electrical conductivity.

Hence, the pillar-layered MOF structure is primarily responsible for facilitating CO_2 adsorption, which makes it suitable for catalysing the CO_2 reduction process. Based on this, artificial CO_2 photoreduction experiments were conducted by irradiating TCPP-Pyz-Co and TCPP-NH_2Pyz-Co with a visible light of 420 nm in a CO_2-saturated CH_3CN/H_2O solution. The

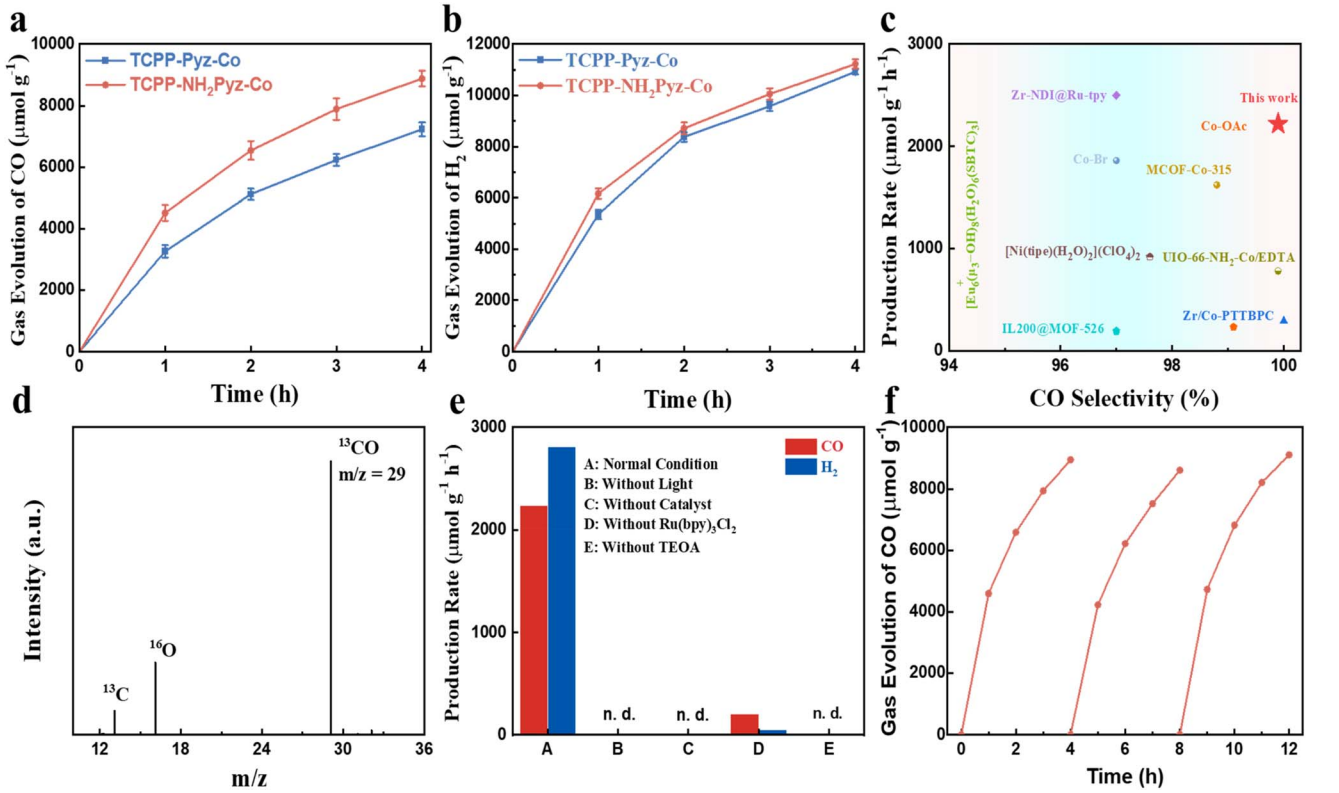

Fig. 4 (a) Photocatalytic CO production and (b) H_2 production activity of TCPP-Pyz-Co and TCPP-NH_2Pyz-Co. (c) The performance comparison of TCPP-Pyz-Co and TCPP-NH_2Pyz-Co and other MOF catalysts in reference literature.[36–43] (d) ^{13}C isotope labelling result based on GC-MS for TCPP-NH_2Pyz-Co. (e) Effect of TCPP-NH_2Pyz-Co photocatalytic CO_2 reduction under different conditions. (f) Recyclability of TCPP-NH_2Pyz-Co in CO_2 photoreduction.

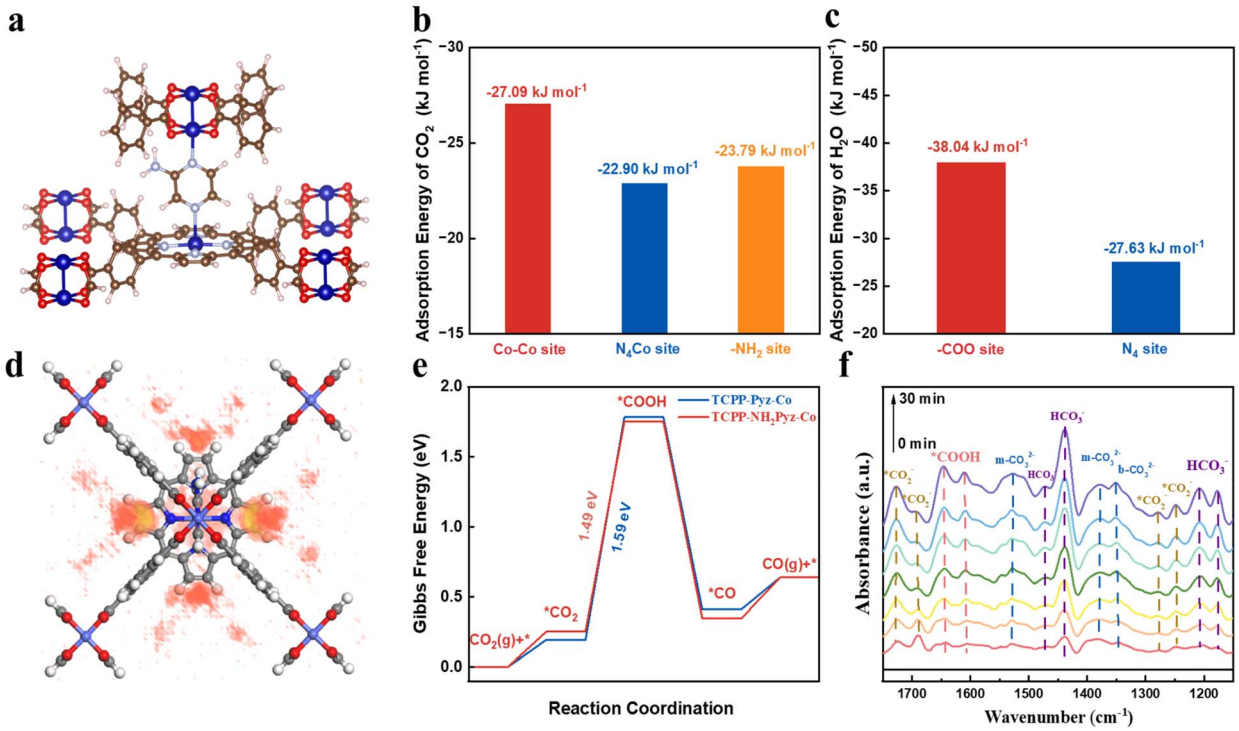

Fig. 5 Photocatalytic mechanism. (a) The model of TCPP-NH_2Pyz-Co. Adsorption energy values for (b) CO_2 and (c) H_2O on various adsorption sites. (d) The CO_2 adsorption density of TCPP-NH_2Pyz-Co. (e) Calculated Gibbs free energy diagrams of the CO_2RR for TCPP-Pyz-Co and TCPP-NH_2Pyz-Co. (f) *In situ* DRIFT spectra over the TCPP-NH_2Pyz-Co catalyst at different irradiation times.

experiments utilized triethanolamine (TEOA) as a sacrificial agent and $Ru(bpy)_3Cl_2$ as a photosensitizer, and gaseous products were quantitatively analysed by gas chromatography (GC). As shown in Fig. 4a, the amount of CO production significantly increased with extended reaction time. The CO yield of TCPP-NH_2Pyz-Co can reach 8885.5 μmol g^{-1} after 4 hours of reaction, corresponding to a production rate of 2221.4 μmol g^{-1} h^{-1}. In comparison, the activity of TCPP-Pyz-Co was slightly lower, with CO production reaching 7230.5 μmol g^{-1} and a rate of 1807.6 μmol g^{-1} h^{-1}. Furthermore, the photocatalytic process also induces the hydrogen evolution reaction (HER) as shown in Fig. 4b. TCPP-NH_2Pyz-Co demonstrated the highest HER catalytic performance producing 11 220.6 μmol g^{-1} of hydrogen gas at a rate of 2805.2 μmol g^{-1} h^{-1}, exhibiting an extremely high hydrogen production rate, which is higher than that of TCPP-Pyz-Co (10 929.0 μmol g^{-1} and 2732.3 μmol g^{-1} h^{-1}). Benefiting from NH_2 functionalization, TCPP-NH_2Pyz-Co exhibited a higher CO production rate compared to its non-NH_2-functionalized counterpart and other published studies[37–43] (Fig. 4c). The isotopic labelling experiments show that ^{13}CO ($m/z = 29$) originated from the reactant of $^{13}CO_2$, which verifies that the generated CO comes from CO_2 rather than from the decomposition of the MOFs (Fig. 4d). Meanwhile, control experiments were conducted (Fig. 4e; the detailed information is provided in Table S4†); the absence of $Ru(bpy)_3Cl_2$ in the control experiments can produce only a little CO, and there is no CO gas produced in the absence of light, catalyst or TEOA. Moreover, TCPP-NH_2Pyz-Co demonstrated excellent robustness and durability during photocatalytic CO_2 reduction reactions. The catalyst maintained consistent performance with minimal activity loss over at least three consecutive test cycles (Fig. 4f). The stability of the TCPP-NH_2Pyz-Co photocatalyst structure was further confirmed by XRD analyses after cyclic testing, which showed no significant structural changes as shown in Fig. S11.†

To elucidate the active sites of the TCPP-NH_2Pyz-Co catalyst, a theoretical investigation was conducted *via* the model of TCPP-NH_2Pyz-Co (Fig. 5a). First, the CO_2 adsorption energies at Co–Co, Co–N_4, and –NH_2 sites were −27.09 kJ mol^{-1}, −22.90 kJ mol^{-1}, and −23.79 kJ mol^{-1} respectively (Fig. 5b and S12†). Notably, these calculated values matched well with the Q_{st} value in Fig. 2f, proving the reliability of the theoretical calculation results. Herein, the Co–Co site exhibits the highest affinity for CO_2 adsorption, while the –NH_2 group also demonstrates a substantial adsorption energy, indicating a strong interaction with CO_2. The incorporation of –NH_2 groups effectively increases the density of potential CO_2 adsorption sites, thereby enhancing the material's overall CO_2 capture performance. In parallel, we examined the H_2O adsorption behaviour at the –COO and N_4 sites. Density functional theory (DFT) calculations indicate adsorption energies of −38.04 kJ mol^{-1} and −27.63 kJ mol^{-1} respectively (Fig. 5c and S13†). This suggests that the –COO site has a stronger affinity for H_2O compared to the Co–N_4 site. Meanwhile, the charge density difference (CDD) analysis illustrates CO_2 adsorption on the Co–Co sites and H_2O adsorption on the –COO groups of MOFs as presented in

Fig. S14 and S15.† The results indicate that the adsorbed CO_2 and H_2O molecules exhibit significant charge interaction with the MOF, leading to effective activation of both species (specifically, the CO_2 adsorption density of TCPP-NH_2Pyz-Co is higher than that of TCPP-Pyz-Co as shown in Fig. 5d and S16†). Furthermore, we established the steps of TCPP-NH_2Pyz-Co reacting with CO_2 in Fig. S17.† Herein, $[Ru(bpy)_3]^{2+}$ first absorbs a photon and reaches the excited state $[Ru(bpy)_3]^{2+}$*. The excited state $[Ru(bpy)_3]^{2+}$* then directly transfers an electron to the Co active site, thereby becoming the oxidized state $[Ru(bpy)_3]^{3+}$. This oxidized state is subsequently reduced back to the ground state $[Ru(bpy)_3]^{2+}$ by the sacrificial hole scavenger (TEOA).

As illustrated in Fig. 5e, TCPP-Pyz-Co and TCPP-NH_2Pyz-Co undergo an adsorption process for CO_2, with the Gibbs free energy change from 0.0 eV to 0.19 eV and 0.25 eV (Fig. S18,† the computational model for each step). Subsequently, *CO_2 overcomes an energy barrier of 1.59 eV and 1.49 eV to obtain a proton (H^+) and an electron (e^-) to form *COOH. Following this, *COOH undergoes a thermodynamically spontaneous dehydration process to generate *CO and finally *CO undergoes a desorption process to convert to CO. In the CO_2RR process, the rate-determining step (RDS) was identified as the *CO_2 hydrogenation process (*CO_2 → *COOH). The energy barrier for the RDS of TCPP-NH_2Pyz-Co is lower than that of TCPP-Pyz-Co, implying the exceptional performance of TCPP-NH_2Pyz-Co in the critical intermediate step in the reduction of CO_2 to CO. Regarding the CO_2 reduction intermediates, we utilized *in situ* FTIR spectroscopy for verification. During illumination, peaks corresponding to *CO_2^-, *COOH, and *CO_3^{2-}/HCO_3^- were observed; the peak at 1348 cm^{-1} is assigned to the bidentate carbonate (b-CO_3^{2-}), and the peaks at 1378 cm^{-1} and 1527 cm^{-1} are assigned to monodentate carbonates (m-CO_3^{2-}). The peaks corresponding to *CO_2^- are at 1247 cm^{-1}, 1278 cm^{-1}, 1689 cm^{-1} and 1727 cm^{-1}, *COOH are at 1610 cm^{-1} and 1646 cm^{-1}, and HCO_3^- are at 1178 cm^{-1}, 1208 cm^{-1}, 1439 cm^{-1} and 1473 cm^{-1}, which are considered key intermediates in the formation and conversion of *CO into CO providing strong evidence for the computational data related to the CO_2 photocatalytic reduction process.[44–46] Collectively, the mechanism proposed for the CO_2RR facilitated by TCPP-NH_2Pyz-Co is that the dinuclear paddlewheel cobalt centers within TCPP-NH_2Pyz-Co serve a dual role during photocatalytic CO_2 reduction. These sites act as both effective catalytic centers and regions with enhanced CO_2 adsorption affinity. The high CO_2 adsorption density on the porphyrin framework corroborates this (Fig. S16†), indicating a notable kinetic advantage for photocatalytic CO_2 reduction. The Lewis base amino groups we introduced play multiple roles: (1) serving as secondary adsorption sites adjacent to the primary adsorption sites, synergistically enhancing CO_2 adsorption capacity of the framework; (2) modulating the band gap of the framework material thereby reducing carrier recombination. This work utilizes a simple Lewis base-introduced ligand strategy to enhance photocatalytic activity by modulating the CO_2 adsorption and band structure of the MOF, providing guiding significance for the design of porphyrin-based high-efficiency CO_2 reduction catalysts.

Conclusions

In summary, we report the design and construction of novel porphyrin-based pillared-layer MOFs using a Lewis base functionalization strategy, successfully fabricating TCPP-Pyz-Co and TCPP-NH_2Pyz-Co photocatalysts. The –NH_2 groups increased the density of high-affinity CO_2 adsorption sites, narrowed the band gap, and broadened the light absorption, promoting efficient charge separation and strengthening interactions with CO_2. The optimized TCPP-NH_2Pyz-Co exhibited superior performance in light-driven CO_2 reduction achieving a CO production rate of 2221.4 μmol g^{-1} h^{-1} (8885.5 μmol g^{-1} over 4 h) and a hydrogen evolution rate of 2805.2 μmol g^{-1} h^{-1}, significantly outperforming its non-functionalized counterpart. DFT calculations demonstrated that TCPP-NH_2Pyz-Co has active sites for CO_2 and H_2O, namely the Co–Co site and –COO site. This work provides a new direction for the design and synthesis of novel MOFs for CO_2 capture and photoreduction applications.

Data availability

The data that support the findings of this study are available from the corresponding author Zihao Xing (xingzh612@nenu.edu.cn) upon reasonable request.

Author contributions

The study was conceptualized by X. G. and Z. X., who also conducted the experiments and drafted the manuscript. Samples were prepared by C. C. and W. L. Initial research planning and experimental setup were contributed by Z. X. SEM analysis was performed by W. X., while N. M. conducted the sample characterization. X. Z. also took the input through discussions. J. C. and Z. X. supervised the research, supported the discussions and facilitated the acquisition of necessary equipment. All authors reviewed and approved the final manuscript. Notably, X. G., C. C., and W. L. made equal contributions to this work.

Conflicts of interest

The authors declare no competing financial interest.

Acknowledgements

This work was supported by the Science and Technology Development Plan Project of Jilin Province, China (20240101192JC). This work was also supported by the National Natural Science Foundation of China (22202037 and 22472023) and the Fundamental Research Funds for the Central Universities (2412024QD014 and 2412023QD019).

Notes and references

1 W. D. Jones, *J. Am. Chem. Soc.*, 2020, **142**, 4955–4957.

2 M. I. Hoffert, K. Caldeira, G. Benford, D. R. Criswell, C. Green, H. Herzog, A. K. Jain, H. S. Kheshgi, K. S. Lackner, J. S. Lewis, H. D. Lightfoot, W. Manheimer, J. C. Mankins, M. E. Mauel, L. J. Perkins, M. E. Schlesinger, T. Volk and T. M. L. Wigley, *Science*, 2002, **298**, 981–987.
3 A. F. Ghoniem, *Prog. Energy Combust. Sci.*, 2011, **37**, 15–51.
4 P. Markewitz, W. Kuckshinrichs, W. Leitner, J. Linssen, P. Zapp, R. Bongartz, A. Schreiber and T. E. Müller, *Energy Environ. Sci.*, 2012, **5**, 7281.
5 K. M. G. Langie, K. Tak, C. Kim, H. W. Lee, K. Park, D. Kim, W. Jung, C. W. Lee, H.-S. Oh, D. K. Lee, J. H. Koh, B. K. Min, D. H. Won and U. Lee, *Nat. Commun.*, 2022, **13**, 7482.
6 G. Liao, G. Ding, B. Yang and C. Li, *Precis. Chem.*, 2024, **2**, 49–56.
7 Y. N. Jing, H. X. Wang, C. Wang, C. Ye, C. H. Tung and L. Z. Wu, *J. Am. Chem. Soc.*, 2025, **147**, 15942–15946.
8 Z.-K. Xin, M.-Y. Huang, Y. Wang, Y.-J. Gao, Q. Guo, X.-B. Li, C.-H. Tung and L.-Z. Wu, *Angew. Chem., Int. Ed.*, 2022, **61**, e202207222.
9 S. Xu, Q. Shen, J. Zheng, Z. Wang, X. Pan, N. Yang and G. Zhao, *Adv. Sci.*, 2022, **9**, 2203941.
10 J. You, M. Xiao, S. Liu, H. Lu, P. Chen, Z. Jiang, W. Shangguan, Z. Wang and L. Wang, *J. Mater. Chem. A*, 2023, **11**, 10149–10154.
11 M. Sai Bhargava Reddy, D. Ponnamma, K. K. Sadasivuni, B. Kumar and A. M. Abdullah, *RSC Adv.*, 2021, **11**, 12658–12681.
12 J. M. Kolle, M. Fayaz and A. Sayari, *Chem. Rev.*, 2021, **121**, 7280–7345.
13 Y. Zou, Y. Huang, D. Si, Q. Yin, Q. Wu, Z. Weng and R. Cao, *Angew. Chem., Int. Ed.*, 2021, **133**, 21083–21088.
14 H. Jiang, C. Cao, W. Liu, H. Zhang, Q. Li, S. Zhu, X. Li, J. Li, J. Chang, W. Hu, Z. Xing, X. Zou and G. Zhu, *J. Energy Chem.*, 2025, **104**, 127–135.
15 C. Zhang, D. Cao, J. Cao, Y. Song, Y. Zheng, L. Luo, J. Liu and Y. Yuan, *Chem.–Eur. J.*, 2024, **31**, 202403733.
16 A. Dai, S. Li, T. Wang, Y. Yang, Y. Tian, X. Jing and G. Zhu, *Chin. Chem. Lett.*, 2022, **34**, 107559.
17 H. Lei, C. Zhu, L. Lin, X. Han, Y. Ding, J. Song, Y. Tian and G. Zhu, *Appl. Catal., B*, 2024, **361**, 124654.
18 A. Li, P. Zhang, E. Kan and J. Gong, *eScience*, 2024, **4**, 100157.
19 J. Yang, P. Li, X. Li, L. Xie, N. Wang, H. Lei, C. Zhang, W. Zhang, Y. Lee, W. Zhang, R. Cao, S. Fukuzumi and W. Nam, *Angew. Chem., Int. Ed.*, 2022, **61**, 21083–21088.
20 L. Zhu, Y. Wang, L. Chen, J. Li, S. Zhou, Q. Yang, X. Wang, C. Tung and L. Wu, *Angew. Chem., Int. Ed.*, 2024, **64**, e202418156.
21 C. Liu, T. de Haas, F. Buda and S. Bonnet, *ACS Catal.*, 2025, **15**, 4681–4697.
22 K. Kosugi, H. Kashima, M. Kondo and S. Masaoka, *Chem. Commun.*, 2022, **58**, 2975–2978.
23 C. Wang, C. Y. Zhu, M. Zhang, Y. Geng, Y. G. Li and Z. M. Su, *J. Mater. Chem. A*, 2020, **8**, 14807–14814.
24 X. Zhao, C.-Y. Zhu, J.-S. Qin, H. Rao, D.-Y. Du, M. Zhang, P. She, L. Li and Z.-M. Su, *Mater. Chem. Front.*, 2024, **8**, 2439–2446.
25 S. Xie, C. Deng, Q. Huang, C. Zhang, C. Chen, J. Zhao and H. Sheng, *Angew. Chem., Int. Ed.*, 2023, **62**, e202216717.
26 C. Wang, X. M. Liu, M. Zhang, Y. Geng, L. Zhao, Y. G. Li and Z. M. Su, *ACS Sustainable Chem. Eng.*, 2019, **7**, 14102–14110.
27 X. Han, Y.-J. Chu, M. Dong, W. Chen, G. Ding, L. L. Wen, K. Z. Shao, Z. Su, M. Zhang, X. Wang and G. G. Shan, *Inorg. Chem.*, 2022, **61**, 5869–5877.
28 A. Bairagi, A. Y. Pereverzev, P. Tinnemans, E. A. Pidko and J. Roithová, *J. Am. Chem. Soc.*, 2024, **146**, 5480–5492.
29 C. M. Boudreaux, D. Nugegoda, W. Yao, N. Le, N. C. Frey, Q. Li, F. Qu, M. Zeller, C. E. Webster, J. H. Delcamp and E. T. Papish, *ACS Catal.*, 2022, **12**, 8718–8728.
30 Z. Wen, S. Xu, Y. Zhu, G. Liu, H. Gao, L. Sun and F. Li, *Angew. Chem., Int. Ed.*, 2022, **134**, e202201086.
31 Y.-L. Liu, Y. Zhao, J. Zhang, Y. Ye and Q. Sun, *J. Solid State Chem.*, 2022, **313**, 123332.
32 W. Wang, W. Chen, W. Yuan, H.-Q. Xu and B. Liu, *Inorg. Chem.*, 2022, **61**, 17937–17942.
33 L. Wang, W. Qiao, H. Liu, S. Li, J. Wu and H. Hou, *Inorg. Chem.*, 2023, **62**, 3817–3826.
34 J. Li, K. Ma, Y. He, S. Ren, C. Li, X.-B. Chen, Z. Shi and S. Feng, *Catal. Sci. Technol.*, 2021, **11**, 7300–7306.
35 L. Wang, Y. Yao, T. Tran, P. Lira, S. P. E. Sternberg, R. Davis, Z. Sun, Q. Lai, S. Toan, J. Luo, Y. Huang, Y. H. Hu and M. Fan, *J. Environ. Manage.*, 2023, **332**, 117398.
36 X. Lai, Y. Shen, S. Gao, Y. Chen, Y. Cui, D. Ning, X. Ji, Z. Liu and L. Wang, *Biosens. Bioelectron.*, 2022, **213**, 114446.
37 B. Wang, W. Li, J. Liu, T. Gan, S. Gao, L. Li, T. Zhang, Y. Zhou, Z. Shi, J. Li, Y. Liu and J. Yu, *Adv. Mater.*, 2025, 2407154.
38 W. Lu, C. E. Tait, G. Avci, X. Li, A. E. Crumpton, P. Shao, C. M. Aitchison, F. Ceugniet, Y. Yao, M. D. Frogley, D. Decarolis, N. Yao, K. E. Jelfs and I. McCulloch, *J. Am. Chem. Soc.*, 2025, **147**, 9056–9061.
39 X. Zhao, Q. Xu, J. Han, W. Zhang, H. Rao, D. Du, P. She and J. Qin, *ACS Appl. Mater. Interfaces*, 2024, **16**, 26272–26279.
40 Z. Qiu, P. Wang, K. Zhang, Y. Zhao and W. Sun, *Inorg. Chem.*, 2024, **63**, 18193–18199.
41 T. Quach, M. Duong, S. Mohan and T. Do, *ACS Appl. Energy Mater.*, 2024, **7**, 8797–8806.
42 K. Sun, Y. Huang, Q. Wang, W. Zhao, X. Zheng, J. Jiang and H.-L. Jiang, *J. Am. Chem. Soc.*, 2024, **146**, 3241–3249.
43 K. L. Xie, L.-P. Wu, Y.-Q. Liao, J. J. Hu, K. Q. Lu, H. R. Wen and J. R. Huo, *Inorg. Chem.*, 2024, **64**, 638–645.
44 M. Cheng, B. Gao, X. Zheng, W. Wu, W. Kong, P. Yan, Z. Wang, B. An, Y. Zhang, Q. Li and Q. Xu, *Appl. Catal., B*, 2024, **353**, 124097.
45 Q. Mo, J. Li, S. Xu, K. Wang, X. Ge, Y. Xiao, G. Wu and F. Xiao, *Adv. Funct. Mater.*, 2022, **33**, 2210332.
46 X. Ma, J. Hu, S. Li, T. Zheng, Y. Gao, Y. Han, H. Pan, Y. Bian and J. Jiang, *Sci. Bull.*, 2025, **70**(14), 2277–2284.

